electronics

Article

# Robust EMPC-Based Frequency-Adaptive Grid Voltage Sensorless Control for an LCL-Filtered Grid-Connected Inverter

**Yubin Kim, Thuy Vi Tran and Kyeong-Hwa Kim ***

Department of Electrical and Information Engineering, Research Center for Electrical and Information Technology, Seoul National University of Science and Technology, 232 Gongneung-ro, Nowon-gu, Seoul 01811, Republic of Korea; dbqls285@gmail.com (Y.K.); tranvithuy@gmail.com (T.V.T.)
* Correspondence: k2h1@seoultech.ac.kr; Tel.: +82-2-970-6406; Fax: +82-2-978-2754

**Abstract:** A robust explicit model predictive control (EMPC)-based frequency-adaptive grid voltage sensorless control is developed for a grid-connected inverter (GCI) via a linear matrix inequality (LMI) approach under the model parametric uncertainties as well as distorted and imbalanced grid voltages. In order to ensure the quality of grid currents injected into the utility grid even when the system model parameters vary, the proposed control scheme is accomplished by an enhanced prediction model rather than the conventional prediction model obtained by fixed parameters. Furthermore, an LMI-based observer is integrated with the disturbance observer to improve the reference tracking performance and to reject disturbances. The proposed observer is employed for the grid frequency-adaptive control without the need for grid voltage sensors. The proposed current controller and observer employ the LMI scheme to maintain a stable and robust operation of the GCI. The discrete-time frequency response and pole-zero map analyses are utilized to examine the system performance including the stability and robustness against parametric uncertainties. Comprehensive simulation and experimental tests as well as theoretical analyses clearly validate the robustness of the proposed control scheme under various harsh test conditions with non-ideal and unexpected grid and system parametric uncertainties.

**Keywords:** disturbance observer; explicit model predictive control (EMPC); grid-connected inverters (GCIs); linear matrix inequality (LMI); uncertainties; voltage sensorless control



**Citation:** Kim, Y.; Tran, T.V.; Kim, K.-H. Robust EMPC-Based Frequency-Adaptive Grid Voltage Sensorless Control for an LCL-Filtered Grid-Connected Inverter. *Electronics* **2024**, *13*, 998. https://doi.org/10.3390/electronics13050998

Academic Editor: Francisco Javier Ruiz-Rodríguez

Received: 29 December 2023
Revised: 28 February 2024
Accepted: 3 March 2024
Published: 6 March 2024



## 1. Introduction

Nowadays, grid-connected inverters (GCIs) are being increasingly developed to facilitate renewable energy generation systems, microgrid or smart grids [1,2]. The GCI systems should operate to effectively transfer the direct current (DC) power from distributed generators to alternative current (AC) power to inject it into the grid even under harsh unexpected grid conditions [3,4]. In particular, reducing the total harmonic distortion (THD) in the GCI current output is one of the most important challenges. In most grid interconnection standards, the harmonic content of the output current should be less than 5% even under a non-ideal grid environment [3].

Commonly, to maximize the inverter power transfer efficiency, the pulse width modulation (PWM) inverters are utilized. To reduce the distortion of the injection currents into the utility grid and to meet the power quality standard [5], low pass filters are an essential component between the GCI and the utility grid. Among these filter types, the inductor-capacitor–inductor (LCL) filter offers superior harmonic suppression capability with reduced filter inductor size compared to others. Nevertheless, the stability of the whole system is easily harmed by the resonance peak of the LCL filter. Therefore, the current control design should be accomplished not only to ensure a good quality of grid-injected currents under several disturbance sources, but also to stabilize the system by damping the resonance phenomenon [6,7].

In addition, the current control method of the GCIs should also consider the disturbance sources which come from both external and internal factors [8]. In particular, the values of LCL filter components may be drifted from the known nominal values due to the manufacturing tolerance, aging effects, or weak grid conditions, which can be considered as internal uncertainties. The external disturbances primarily arise from the severe distortion or unbalanced behavior of the grid voltages [9,10].

Since power conversion systems should be operated with high efficiency as well as improved flexibility and profitability, many authors have a tendency to focus on robust algorithm, adaptive algorithm or learning algorithm to obtain the stabilization of the entire system even in the presence of harsh conditions of the utility grid [6,11–16]. The linear quadratic regulators (LQR) were proposed as a method to determine the optimal controller gains by means of a cost function minimization [17,18]. Compared to the pole placement method [9], the LQR method offers the advantage of achieving an optimal feedback gain set by choosing appropriate weighting factors. However, the LQR controllers commonly require the user's experience and knowledge in choosing proper weighting factors. Other approaches in [6,11] present the linear matrix inequality (LMI) method to optimally generate the control gains, in which the Lyapunov stability condition is employed to guarantee robust stability and good performance despite the model inaccuracy. Even though these studies provide satisfactory performance under parametric uncertainties, several external disturbances such as grid voltage imbalance degrade the current controller operations. Another approach [12] employs H∞ control to cope with the additional grid impedance caused by the weak grid. The robust performance of H∞ control is guaranteed even under parametric uncertainties. However, this study did not consider the grid voltage imbalances and frequency fluctuations of the real grid.

As a method to consider the system constraints effectively and to yield a fast output response, model predictive control (MPC) has been studied. If all the parameters in the system are well-known, the MPC generally provides an excellent controller performance as well as an accurate output tracking [1,10,13–15]. However, the performance of the MPC depends on computationally intensive and accurate system models and parameters. In addition, the system stability of the MPC-based GCI is affected by parametric uncertainties and the weak grid. The LMI-based MPC method was also proposed in [6,16] to solve the problem of the conventional MPC. Although several non-ideal grid conditions were addressed, the control scheme in [6] does not consider grid voltage sensorless control. Moreover, it does not consider severe parametric uncertainty conditions. In [16], the closed-loop system analyses were represented to verify the robust stability. However, severe grid disturbance such as grid harmonics and imbalanced grid voltages was not addressed.

In order to achieve robust stability, low computational burden, high efficiency, and good tracking performance despite model inaccuracies as well as external disturbances, this study investigates a robust explicit MPC (EMPC)-based frequency-adaptive current controller of a GCI system without the grid voltage sensors. Because the proposed control scheme does not require additional sensing devices for realizing the active damping method, integral term, and second-order harmonic compensation term, the computational burden to implement the proposed scheme can be reduced, while maintaining a good tracking performance.

The proposed study is improved in two aspects. First, the LMI-based MPC algorithm is employed by an LQR-based prediction model in order to improve the stability of the GCI system under parametric uncertainties and to reduce the computational burden in comparison to the conventional MPC algorithm in [6]. In the proposed scheme, an LQR-based prediction model is obtained with state and control input at time step $k$ to predict the overall prediction horizon. Second, to realize a current controller without the grid voltage sensors, the proposed controller deploys an LMI-based resonant extended state observer with the grid frequency adaptation to guarantee high estimation accuracy for grid voltages and system state variables with various grid conditions. In particular, the proposed LMI-based observer also integrates a disturbance observer to ensure a good performance of the resonant extended state observer by rejecting the influence of disturbances. Comprehensive simulation and experimental results as well as analyses effectively validate the robustness of the proposed controller under several harsh conditions such as internal parametric uncertainties as well as unexpected grid distortion and an imbalanced grid.

## 2. System of a GCI

### *2.1. Model of a GCI with LCL Filter*

Figure 1 depicts the power circuit of a three-phase LCL-filtered GCI controlled by the proposed scheme which employs only the measurement of dc-link voltage and the grid-side currents. In Figure 1, $L_1$ and $L_2$ are the filter inductances in inverter-side and grid-side, respectively, $R_1$ and $R_2$ are the filter resistances in inverter-side and grid-side, respectively, $L_g$ is the grid inductance, and $C_f$ is the filter capacitance. In this figure, $\mathbf{i}_1$ is the inverter-side currents, $\mathbf{v}_c$ is the filter capacitor voltages, $\mathbf{i}_2$ is the grid-side currents, $\mathbf{u}$ is the inverter voltages, $\mathbf{e}$ is the utility grid voltages, $\mathbf{d}$ is the disturbance, and the symbol '^' denotes the estimated quantity. The voltage $\mathbf{v}_{PCC}$ denotes the point of common coupling (PCC) voltages which are the same with the utility grid voltages $\mathbf{e}$ if the grid impedance does not exist. Variable $\tilde{\omega}$ is the grid angular frequency of the moving average filter (MAF) that is deployed to remove the frequency fluctuation obtained from the conventional phase lock loop (PLL) under grid voltage distortion. The superscripts '*qd*' represent the *qd*-axis variables in the synchronous reference frame (SRF), 'αβ' represents the variables in the stationary frame, and '*abc*' represents the phase variables. To apply the reference voltages to GCI, the space vector pulse width modulation (SVPWM) scheme is employed in the proposed scheme.

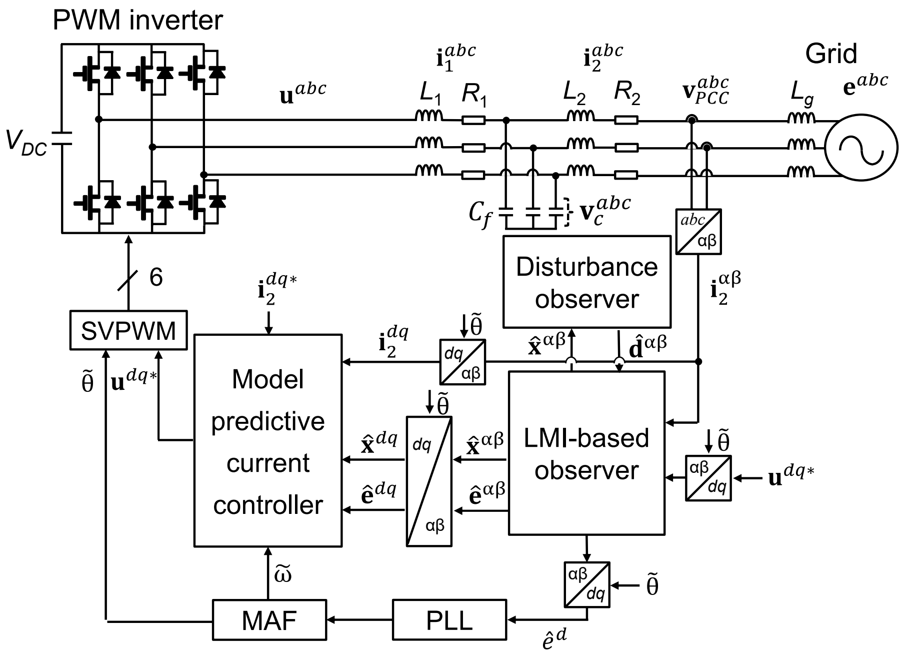


**Figure 1.** Power circuit of LCL-filtered GCI with the proposed control scheme.

In a state-space matrix form, the GCI system can be presented in the SRF by the continuous-time model as follows [6]:

$$\dot{\mathbf{x}}(t) = \mathbf{A}\,\mathbf{x}(t) + \mathbf{B}\,\mathbf{u}\,(t) + \mathbf{D}\,\mathbf{e}\,(t) + \mathbf{d}\,(t) \tag{1}$$

$$\mathbf{y}(t) = \mathbf{C}\,\mathbf{x}(t) \tag{2}$$

where $\mathbf{x} = [i_2^q, i_2^d, i_1^q, i_1^d, v_c^q, v_c^d]^T$ is the state, $\mathbf{u} = [v_i^q, v_i^d]^T$ is the control input, $\mathbf{e} = [e^q,\ e^d]^T$ is the grid voltage vector, and $\mathbf{d} = [d_1, d_2, d_3, d_4, d_5, d_6]^T$ is the disturbance vector, and

$$\mathbf{A} = \begin{bmatrix} -R_2/L_2 & -\omega & 0 & 0 & 1/L_2 & 0 \\ \omega & -R_2/L_2 & 0 & 0 & 0 & 1/L_2 \\ 0 & 0 & -R_1/L_1 & -\omega & -1/L_1 & 0 \\ 0 & 0 & \omega & -R_1/L_1 & 0 & -1/L_1 \\ -1/C_f & 0 & 1/C_f & 0 & 0 & -\omega \\ 0 & -1/C_f & 0 & 1/C_f & \omega & 0 \end{bmatrix} \quad (3)$$

$$\mathbf{B} = \begin{bmatrix} 0 & 0 \\ 0 & 0 \\ 1/L_1 & 0 \\ 0 & 1/L_1 \\ 0 & 0 \\ 0 & 0 \end{bmatrix}, \mathbf{D} = \begin{bmatrix} -1/L_2 & 0 \\ 0 & -1/L_2 \\ 0 & 0 \\ 0 & 0 \\ 0 & 0 \\ 0 & 0 \end{bmatrix}, \mathbf{C} = \begin{bmatrix} 1 & 0 & 0 & 0 & 0 & 0 \\ 0 & 1 & 0 & 0 & 0 & 0 \end{bmatrix} \quad (4)$$

$\omega$ is the angular frequency of the grid.

### 2.2. System Modeling under Parametric Uncertainties

Because of manufacturing tolerance in real filter parameters, the parameter values are greater than or less than the nominal values. In addition, the weak grid causes the grid impedance value to fluctuate. In this work, the LCL filter parameters are assumed to have uncertainties within certain ranges defined as follows:

$$L_{2,\min} \leq L_2 \leq L_{2,\max} = L_2/\delta_1 \leq L_2 \leq L_2\delta_1 \quad (5)$$

$$L_{1,\min} \leq L_1 \leq L_{1,\max} = L_1/\delta_2 \leq L_1 \leq L_1\delta_2 \quad (6)$$

$$C_{f,\min} \leq C_f \leq C_{f,\max} = C_f/\delta_2 \leq C_f \leq C_f\delta_2 \quad (7)$$

where $\delta_1$ and $\delta_2$ are the uncertainty coefficients of the LCL filter $(\delta_1 > 1,\ \delta_2 > 1)$. Those ranges are expressed as a convex combination of eight vertices as follows:

$$\boldsymbol{\kappa} = \left\{ \sum_{k=1}^{2^3} \psi_k(\mathbf{A}_k, \mathbf{B}_k, \mathbf{C}_k) | \sum_{k=1}^{2^3} \psi_k = 1, \psi_k \geq 0 \right\}. \quad (8)$$

The polytopic uncertainty set $\boldsymbol{\kappa}$ contains the uncertain system matrices which are obtained by considering a combination of eight extreme values.

### 2.3. Model Discretization

To discretize uncertain systems in the continuous-time, the zero-order hold approach is used in the proposed controller with the sampling period $T_s$ for all vertices given in (1) and (8) as

$$\mathbf{x}(k+1) = \mathbf{A}_{di}\mathbf{x}(k) + \mathbf{B}_{di}\mathbf{u}(k) + \mathbf{D}_{di}\mathbf{e}(k) + \mathbf{d}_d \quad (9)$$

$$\mathbf{y}(k) = \mathbf{C}_{di}\mathbf{x}(k) \quad (10)$$

where

$$\mathbf{A}_{di} = e^{\mathbf{A}_i T_s} = \mathbf{I} + \frac{\mathbf{A}_i T_s}{1!} + \frac{\mathbf{A}_i^2 T_s^2}{2!} + \dots \quad (11)$$

$$\mathbf{B}_{di} = \left( \int_0^{T_s} e^{\mathbf{A}_i T_s} d\tau \right) \mathbf{B}_i = \mathbf{A}_i^{-1}(\mathbf{A}_{di} - \mathbf{I})\mathbf{B}_i \quad (12)$$

$$\mathbf{D}_{di} = \left( \int_0^{T_s} e^{\mathbf{A}_i T_s} d\tau \right) \mathbf{D}_i = \mathbf{A}_i^{-1}(\mathbf{A}_{di} - \mathbf{I})\mathbf{D}_i \quad (13)$$

$$\mathbf{C}_{di} = \mathbf{C} \quad (14)$$

for $i = 1, 2, 3, \cdots, 8$.

## 3. Proposed Current Control Design with LMI-Based MPC

The MPC is known to be an optimal control strategy that derives control inputs using predicted future states and feedback information. Nevertheless, the optimization procedure must be repeated using new measurement values in each sampling period; thus, the online implementation causes a heavy burden of computation on the digital signal processor (DSP). Moreover, since the performance of the conventional MPC technique mainly depends on the accuracy of the plant model, this scheme is weak under unexpected uncertainties or disturbance [1,13–15]. To address such limitations, the proposed EMPC is combined with the LMI tool in this paper to reduce computational burden as well as to ensure satisfied output performance and robustness against both parametric uncertainties and grid disturbances.

### 3.1. Converional Prediction Model

In the conventional scheme, the inverter model is used to calculate the prediction of future states with the MPC. Using the system state (9), the prediction model from the time step $(k+1)$ to $(k+N)$ is given as:

$$\begin{aligned}\begin{bmatrix} \mathbf{x}(k+1) \\ \mathbf{x}(k+2) \\ \mathbf{x}(k+3) \\ \vdots \end{bmatrix} &= \begin{bmatrix} \mathbf{A}_{d,6\times6} \\ \mathbf{A}^2_{d,6\times6} \\ \mathbf{A}^3_{d,6\times6} \\ \vdots \end{bmatrix} \begin{bmatrix} \mathbf{x}(k) \\ \mathbf{x}(k) \\ \mathbf{x}(k) \\ \vdots \end{bmatrix} + \begin{bmatrix} \mathbf{B}_{d,6\times6} & \mathbf{0} & \mathbf{0} & \cdots \\ \mathbf{A}_{d,6\times6}\mathbf{B}_{d,6\times6} & \mathbf{B}_{d,6\times6} & \mathbf{0} & \cdots \\ \mathbf{A}^2_{d,6\times6}\mathbf{B}_{d,6\times6} & \mathbf{A}_{d,6\times6}\mathbf{B}_{d,6\times6} & \mathbf{B}_{d,6\times6} & \cdots \\ \vdots & \vdots & \vdots & \ddots \end{bmatrix} \begin{bmatrix} \mathbf{u}(k) \\ \mathbf{u}(k+1) \\ \mathbf{u}(k+2) \\ \vdots \end{bmatrix} \\ &+ \begin{bmatrix} \mathbf{D}_{d,6\times6} & \mathbf{0} & \mathbf{0} & \cdots \\ \mathbf{A}_{d,6\times6}\mathbf{D}_{d,6\times6} & \mathbf{D}_{d,6\times6} & \mathbf{0} & \cdots \\ \mathbf{A}^2_{d,6\times6}\mathbf{D}_{d,6\times6} & \mathbf{A}_{d,6\times6}\mathbf{D}_{d,6\times6} & \mathbf{D}_{d,6\times6} & \cdots \\ \vdots & \vdots & \vdots & \ddots \end{bmatrix} \begin{bmatrix} \mathbf{e}(k) \\ \mathbf{e}(k+1) \\ \mathbf{e}(k+2) \\ \vdots \end{bmatrix}\end{aligned} \tag{15}$$

or

$$\mathbf{x}_p(k+N) = \mathbf{A}_p\mathbf{x}_p(k) + \mathbf{B}_p\mathbf{u}_p(k+N) + \mathbf{D}_p\mathbf{e}_p(k+N) \tag{16}$$

$$\mathbf{u}_p(k) = -\begin{bmatrix} \mathbf{K}_L & \cdots & \mathbf{0} \\ \vdots & \ddots & \vdots \\ \mathbf{0} & \cdots & \mathbf{K}_L \end{bmatrix} \mathbf{x}(k) \tag{17}$$

where $\mathbf{x}_p$ is the future prediction states, $\mathbf{u}_p$ is the control inputs, $\mathbf{e}_p$ is the grid voltages, $N$ is the prediction horizon length, and $\mathbf{K}_L$ is the prediction model gain.

### 3.2. LQR-Based Prediction Model

The conventional prediction model does not take into account the model parameter variations and uncertainties. The performance of the conventional MPC may be rapidly degraded under both internal and external disturbances affecting the system in practical applications. To address these effects, an LQR-based prediction model is presented to reduce the dependence on parameter values of the prediction model. Also, the proposed prediction model has the advantage of requiring only a system state at the current time $k$.

The LQR-based prediction model provides an optimal prediction model gain $\mathbf{K}_L$ in (17) by means of the minimization of the quadratic cost function as

$$\mathbf{J}_p = \textstyle\sum_{l=0}^{\infty} \mathbf{x}_p^T(k+l)\ \mathbf{Q}_p\mathbf{x}_p(k+l) + \mathbf{u}_p^T(k+l)\mathbf{R}_p\mathbf{u}_p(k+l) \tag{18}$$

where $\mathbf{Q}_p$ and $\mathbf{R}_p$ denote positive definite and semidefinite matrices, respectively. To generate the $\mathbf{u}_p$ in (17) in closed-loop form, the discrete-time algebraic Riccati equation (ARE) can be determined as follows:

$$\mathbf{P}_p = \mathbf{Q}_p + \mathbf{A}_p^T\mathbf{P}_p\mathbf{A}_p - \mathbf{A}_p^T\mathbf{P}_p\mathbf{B}_p\left(\mathbf{R}_p + \mathbf{B}_p^T\mathbf{P}_p\mathbf{B}_p\right)^{-1}\mathbf{B}_p^T\mathbf{P}_p\mathbf{A}_p \tag{19}$$

where $\mathbf{P}_p$ denotes the solution of the discrete-time ARE. The LQR can easily reach optimal control with minimal control effort. The closed-loop form $\mathbf{A}_{cl} = \mathbf{A}_d - \mathbf{K}_L\mathbf{B}_d$ can be obtained using the control input (17). The LQR-based prediction model from time step ($k$ + 1) to ($k$ + $N$) which constitutes the enhanced prediction model is determined as

$$\begin{bmatrix} \mathbf{x}(k+1) \\ \mathbf{x}(k+2) \\ \mathbf{x}(k+3) \\ \vdots \\ \mathbf{x}(k+N) \end{bmatrix} = \begin{bmatrix} \mathbf{A}_{cl} \\ \mathbf{A}_{cl}^2 \\ \mathbf{A}_{cl}^3 \\ \vdots \\ \mathbf{A}_{cl}^N \end{bmatrix} \begin{bmatrix} \mathbf{x}(k) \\ \mathbf{x}(k) \\ \mathbf{x}(k) \\ \vdots \\ \mathbf{x}(k) \end{bmatrix} + \begin{bmatrix} \mathbf{D}_d & \mathbf{0} & \mathbf{0} & \cdots \\ \mathbf{A}_{cl}\mathbf{D}_d & \mathbf{D}_d & \mathbf{0} & \cdots \\ \mathbf{A}_{cl}^2\mathbf{D}_d & \mathbf{A}_{cl}\mathbf{D}_d & \mathbf{D}_d & \cdots \\ \vdots & \vdots & \vdots & \ddots \\ \mathbf{A}_{cl}^{N-1}\mathbf{D}_d & \mathbf{A}_{cl}^{N-2}\mathbf{D}_d & \mathbf{A}_{cl}^{N-3}\mathbf{D}_d & \cdots \end{bmatrix} \begin{bmatrix} \mathbf{e}(k) \\ \mathbf{e}(k) \\ \mathbf{e}(k) \\ \vdots \\ \mathbf{e}(k) \end{bmatrix} \tag{20}$$

The LQR-based prediction model generation removes the requirement for future inputs unlike the conventional prediction model (15) and greatly simplifies computational process. The unknown grid voltage in (9) can be considered to be constant as follow [16]:

$$\mathbf{e}(k) = \mathbf{e}(k+1). \tag{21}$$

The proposed LQR-based prediction model is developed to enhance the robustness against the parametric uncertainties without requiring self-tuning processes.

### 3.3. Explicit Model Predictive Control

By substituting the grid-side current references $i_2^{q*}$, $i_2^{d*}$ and the estimated values of grid voltages $\hat{e}^q$, $\hat{e}^d$ in (9), the reference state and control are obtained in a steady state as

$$v_c^{q*} = R_2 i_2^{q*} + L_2\widetilde{\omega} i_2^{d*} + \hat{e}^q \tag{22}$$

$$v_c^{d*} = R_2 i_2^{d*} - L_2\widetilde{\omega} i_2^{q*} + \hat{e}^d \tag{23}$$

$$i_1^{q*} = i_2^{q*} + C_f\widetilde{\omega} v_c^{d*} \tag{24}$$

$$i_1^{d*} = i_2^{d*} - C_f\widetilde{\omega} v_c^{q*} \tag{25}$$

$$u^{q*} = R_1 i_1^{q*} + L_1\widetilde{\omega} i_1^{d*} + v_c^{q*} \tag{26}$$

$$u^{d*} = R_1 i_1^{d*} - L_1\widetilde{\omega} i_1^{q*} + v_c^{d*} \tag{27}$$

where $i_1^{q*}$ and $i_1^{d*}$ are the references of inverter-side currents, and $v_c^{q*}$ and $v_c^{d*}$ are the references of capacitance voltages.

To design the MPC, a cost function $\mathbf{J}_{MP}$ is constructed as follows:

$$\mathbf{J}_{MP} = \sum_{j=1}^{N} [\mathbf{e}_x(k+j)]^T\mathbf{Q}_{MP}[\mathbf{e}_x(k+j)] + [\mathbf{e}_u(k+j)]^T\mathbf{R}_{MP}[\mathbf{e}_u(k+j)] \tag{28}$$

where $\mathbf{e}_x(k) = \hat{\mathbf{x}}(k) - \mathbf{x}^*(k)$, $\mathbf{e}_u(k) = \mathbf{u}(k) - \mathbf{u}^*(k)$, $\mathbf{x}^* = [i_2^{q*}, i_2^{d*}, i_1^{q*}, i_1^{d*}, v_c^{q*}, v_c^{d*}]^T$ represents the reference of state, $\mathbf{u}^* = [u^{q*}, u^{d*}]^T$ is the reference of the control input, $\mathbf{Q}_{MP}$ and $\mathbf{R}_{MP}$ are a symmetric positive-definite and semidefinite weighting matrices, respectively. To obtain the MPC input $\mathbf{u}(k)$, the first derivative of $\mathbf{J}_{MP}(k)$ is considered as

$$\frac{\partial \mathbf{J}_{MP}(\mathbf{x}(k), \mathbf{u}(k))}{\partial \mathbf{u}(k)} = 0 \tag{29}$$

The MPC control input is derived from (28) as

$$\mathbf{u}(k) = \left(\mathbf{B}_M^T \begin{bmatrix} \mathbf{Q}_{MP} & \cdots & \mathbf{0} \\ \vdots & \ddots & \vdots \\ \mathbf{0} & \cdots & \mathbf{Q}_{MP} \end{bmatrix}\right) \mathbf{A}_M \left[ \mathbf{B}_M^T \begin{bmatrix} \mathbf{Q}_{MP} & \cdots & \mathbf{0} \\ \vdots & \ddots & \vdots \\ \mathbf{0} & \cdots & \mathbf{Q}_{MP} \end{bmatrix} \mathbf{B}_M + \mathbf{R}_{MP} \right]^{-1} \mathbf{e}_x + \mathbf{u}^*(k) \tag{30}$$

or

$$\mathbf{u}(k) = \mathbf{K}_{MP}\mathbf{e}_x(k) + \mathbf{u}^*(k) \tag{31}$$

where $\mathbf{A}_M = \begin{bmatrix} \mathbf{A}_{cl} \\ \mathbf{A}_{cl}^2 \\ \mathbf{A}_{cl}^3 \\ \vdots \\ \mathbf{A}_{cl}^N \end{bmatrix}, \mathbf{B}_M = \begin{bmatrix} \mathbf{D}_d & \mathbf{0} & \mathbf{0} & \cdots \\ \mathbf{A}_{cl}\mathbf{D}_d & \mathbf{D}_d & \mathbf{0} & \cdots \\ \mathbf{A}_{cl}^2\mathbf{D}_d & \mathbf{A}_{cl}\mathbf{D}_d & \mathbf{D}_d & \cdots \\ \vdots & \vdots & \vdots & \ddots \\ \mathbf{A}_{cl}^{N-1}\mathbf{D}_d & \mathbf{A}_{cl}^{N-2}\mathbf{D}_d & \mathbf{A}_{cl}^{N-3}\mathbf{D}_d & \cdots \end{bmatrix}$.

At each time step k, the EMPC selects the best MPC input signal to minimize the cost function as in (29). As a result, the errors between system states and references values $\mathbf{e}_x(k)$ are also minimized, and the excellent reference tracking performance is achieved.

### *3.4. LMI-Based Parameter Derivation*

To achieve the reference tracking objective of zero steady-state error, the cost function in (28) is minimized. In the conventional full-state feedback controller described in [19], additional integral control terms and resonant control terms tuned at the 2nd order harmonic are included in the GCI model to guarantee a zero-output tracking error even in the presence of the grid voltage imbalances. Evidently, this approach increases the computation burden due to the augmentation of multiple control terms. On the contrary, the proposed method ensures a good performance of reference tracking regardless of balanced or imbalanced utility grid voltage by means of the control input in (30) without using any additional augmentation of control components.

One of the challenging parts in the MPC design is to choose the proper weighting matrices in (28), and to maintain a stability for a parametric uncertain system. To address this concern, the LMI method is incorporated into the MPC design, which ensures robustness under parametric uncertainty boundaries. Moreover, it is also easier to systematically find a weighting matrix $\mathbf{Q}_{MP}$ in (28). To design the LMI-based MPC, the Lyapunov function is formed as

$$\mathbf{V}(k) = \mathbf{e}_x(k)^T\mathbf{Q}_{MP}\mathbf{e}_x(k) \tag{32}$$

Minimizing the cost function (28) is difficult when the polytopic uncertainties are included in system model. To overcome this limitation, the LQR-LMI method in [7] is deployed for the purpose of ensuring the robust stability of the system. In particular, the LMI approach ensures system stability and robust performance if, and only if

$$\mathbf{V}(k+1) - \mathbf{V}(k) \leq -\left[\mathbf{e}_x(k)^T\mathbf{Q}_L\mathbf{e}_x(k) + \mathbf{e}_u(k)^T\mathbf{R}_L\mathbf{e}_u(k)\right]. \tag{33}$$

From (33), the LMI is derived as follows:

$$(\mathbf{A}_{di} + \mathbf{B}_{di}\mathbf{\Phi})^T\mathbf{Q}_{MP}(\mathbf{A}_{di} + \mathbf{B}_{di}\mathbf{\Phi}) - \mathbf{Q}_{MP} < -\mathbf{Q}_L - \mathbf{\Phi}^T\mathbf{R}_L\mathbf{\Phi} \tag{34}$$

where $\mathbf{Q}_L$ and $\mathbf{R}_L$ denote the weighting matrices for the LQR-LMI method, $\mathbf{\Phi}$ is the gain determined in order that the Lyapunov function monotonically decreases. Multiplying the definite matrix $\mathbf{Y}\left(\mathbf{Y} = \mathbf{Q}_{MP}^{-1}\right)$ on both sides of (34) yields

$$\mathbf{Y}^T - \mathbf{Y}^T\mathbf{Q}_L\mathbf{Y} - (\mathbf{\Phi}\mathbf{Y})^T\mathbf{R}_L\mathbf{\Phi}\mathbf{Y} - (\mathbf{A}_{di}\mathbf{Y} + \mathbf{B}_{di}\mathbf{\Phi}\mathbf{Y})^T\mathbf{Q}_{MP}(\mathbf{A}_{di}\mathbf{Y} + \mathbf{B}_{di}\mathbf{\Phi}\mathbf{Y}) \geq 0 \tag{35}$$

Utilizing the Schur complement to (35) yields

$$\mathbf{Z} = \begin{bmatrix} \mathbf{Y} & (\mathbf{\Phi Y})^T & \mathbf{T}_i^T & \mathbf{Y}^T \\ \mathbf{\Phi Y} & \mathbf{R}_L^{-1} & \mathbf{0} & \mathbf{0} \\ \mathbf{0} & \mathbf{0} & \mathbf{Y} & \mathbf{0} \\ \mathbf{Y} & \mathbf{0} & \mathbf{0} & \mathbf{Q}_L^{-1} \end{bmatrix} \geq 0 \tag{36}$$

where $\mathbf{T}_i = \mathbf{A}_{di}\mathbf{Y} + \mathbf{B}_{di}\mathbf{\Phi Y}$ for $i$ = 1, 2, 3, $\cdots$, 8. Lastly, the LMI problem in the sense of Lyapunov theory over the infinite horizon is stable if, and only if

$$\sum_{k=0}^{\infty}[\mathbf{V}(k+1) - \mathbf{V}(k)] = \mathbf{V}(\infty) - \mathbf{V}(0) \leq \sum_{k=0}^{\infty} -\left[\mathbf{e}_x(k)^T\mathbf{Q}_L\mathbf{e}_x(k) + \mathbf{e}_u(k)^T\mathbf{R}_L\mathbf{e}_u(k)\right] \tag{37}$$

As presented in [11], $\mathbf{V}(\infty)$ is converged to zero in a stable controlled system. Thus, it yields that the cost function of (37) should be less than $\mathbf{V}(0)$. If $\sigma$ denotes an upper bound of $\mathbf{V}(0)$, the LMI holds as

$$\mathbf{V}(0) = \mathbf{e}_x(0)^T\mathbf{Q}_{MP}\mathbf{e}_x(0) \leq \sigma. \tag{38}$$

Then, a weighting matrix $\mathbf{Q}_{MP}$ in (28) is obtained by the solution of the optimization problem as

$$\underset{\mathbf{Y}}{\mathbf{MIN}}\ \sigma \quad \text{subject to} \begin{bmatrix} \mathbf{Z} & \mathbf{0} & \mathbf{0} \\ \mathbf{0} & \sigma & \mathbf{e}_x^T(0) \\ \mathbf{0} & \mathbf{e}_x(0) & \mathbf{Y} \end{bmatrix} \geq 0 \tag{39}$$

where $\mathbf{Z}$ denotes the matrix in (36). In (28), $\mathbf{Q}_{MP} = \mathbf{Y}^{-1}$ is obtained by the LMI optimization method. The benefit of this scheme is that the solution ensures strong robustness and stability under system uncertainties.

### *3.5. Distorted Harmonic Compensation*

To eliminate the negative impacts from the distortion in grid voltages and to assure high-quality sinusoidal currents into the utility grid, the proportional resonance (PR) controllers with grid frequency-adaptive capability are constructed in parallel with the proposed EMPC. The grid harmonic voltages in the 5th, 7th, 11th, and 13th orders in the '*abc*' frame are effectively removed only with light computational burden with two PR controllers which are designed at the 6th and 12th orders in the SRF. The frequency-adaptive PR controllers are expressed as [20]:

$$PR_n(k) = \mathbf{L}_{nPR}\frac{z^2 + \left(2 - \frac{(n\tilde{\omega}T_s)^2}{2} + \frac{(n\tilde{\omega}T_s)^4}{24}\right)z + \left(1 - \frac{(n\tilde{\omega}T_s)^2}{2} + \frac{(n\tilde{\omega}T_s)^4}{24}\right)}{z^2 - 2\cos(n\tilde{\omega}T_s)z + 1} \tag{40}$$

where $n$ = 6, 12 is the order of harmonics, $\mathbf{L}_{nPR}$ is the PR gain for 6th and 12th order. In order to avoid the degradation of harmonic suppression under the utility grid frequency variation, the filtered grid frequency $\tilde{\omega}$ is updated in the PR controllers.

## 4. Frequency-Adaptive Grid Voltage Sensorless Controller

Figure 2 shows the proposed frequency-adaptive grid voltage sensorless controller, in which $\varepsilon^{dq} = \mathbf{r}^{dq} - \mathbf{y}^{dq}$ denotes the grid current error, $\mathbf{r}^{dq} = [i_2^{q*}, i_2^{d*}]^T$, $\mathbf{y}^{dq} = [i_2^q, i_2^d]^T$, and $\mathbf{L}_1$ and $\mathbf{L}_h$ are the gains of the proposed LMI-based observer.

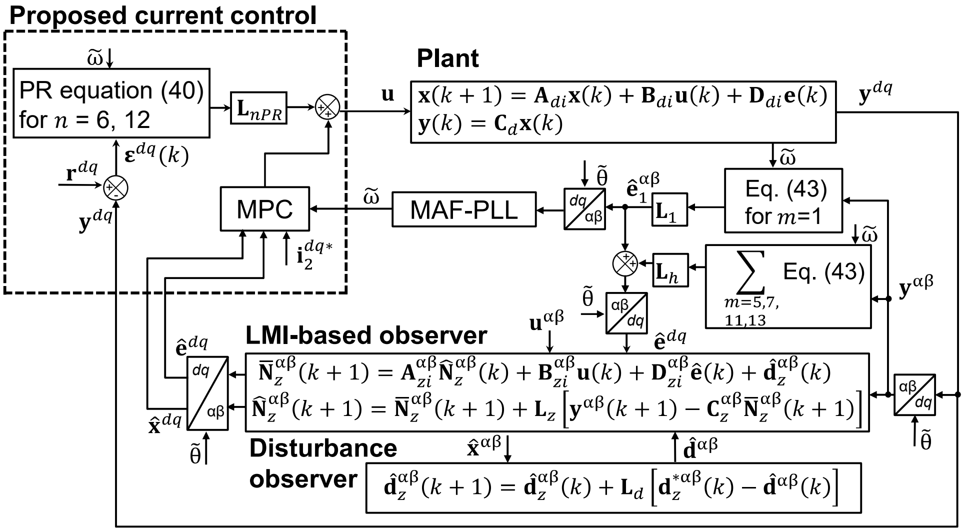


**Figure 2.** Structure of a frequency-adaptive grid voltage sensorless controller.

### *4.1. LMI-Based Observer with Disturbance Observer for Sensorless Control*

In this section, an LMI-based observer which mitigates the influence of the parametric uncertainties, is deployed to estimate the grid voltages as well as entire system states. From the grid voltage estimate, the phase angle and angular frequency of the utility grid are extracted. Finally, the estimated angular frequency information is used to adjust the LMI-based observer model. In addition, the extracted grid frequency is also updated in the controller and harmonic compensator to prevent performance degradation under frequency fluctuations. Because the proposed LMI-based observer is designed in the stationary frame, the system model is discretized easily irrespective of frequency variation. For the LMI-based observer algorithm, the resonant model is adopted, which is represented in z-domain transfer function as follows [21]:

$$G_m = \frac{z^2 - \cos(m\,\tilde{\omega}T_s)z}{z^2 - 2\cos(m\,\tilde{\omega}T_s)z + 1} \tag{41}$$

where $m$ is the harmonic order for $m$ = 1, 5, 7, 11, 13. In state-space, the transfer function in (41) is written as follows:

$$\begin{bmatrix} \hat{h}_m^{\alpha}(k+1) \\ \hat{h}_m^{\beta}(k+1) \end{bmatrix} = \begin{bmatrix} 2\cos(m\,\tilde{\omega}T_s) & 1 \\ -1 & 0 \end{bmatrix} \begin{bmatrix} \hat{h}_m^{\alpha}(k) \\ \hat{h}_m^{\beta}(k) \end{bmatrix} + \begin{bmatrix} L_h^{\alpha}\cos(m\,\tilde{\omega}T_s) \\ -L_h^{\beta} \end{bmatrix} \left[\mathbf{y}^{\alpha\beta}(k+1) - \mathbf{C}_{di}^{\alpha\beta}\overset{-\alpha\beta}{\mathbf{x}_{di}}(k+1)\right] \tag{42}$$

where $L_h$ is the resonant observer gain. The estimate of the utility grid voltage is constructed by adding the fundamental component with individual harmonic components as follows:

$$\hat{\mathbf{e}}^{\alpha\beta}(k) = \sum\nolimits_m \hat{\mathbf{h}}_m^{\alpha\beta}(k), \text{ for } m = 1,\ 5,\ 7,\ 11,\ 13. \tag{43}$$

The proposed LMI-based observer is augmented into the GCI state model in the stationary frame as follows:

$$\overset{-\alpha\beta}{\mathbf{N}_z}(k+1) = \mathbf{A}_{zi}^{\alpha\beta}\,\hat{\mathbf{N}}_z^{\alpha\beta}(k) + \mathbf{B}_{zi}^{\alpha\beta}\,\mathbf{u}(k) + \mathbf{D}_{zi}^{\alpha\beta}\,\hat{\mathbf{e}}(k) + \hat{\mathbf{d}}_z^{\alpha\beta}(k). \tag{44}$$

$$\hat{\mathbf{N}}_z^{\alpha\beta}(k+1) = \overset{-\alpha\beta}{\mathbf{N}_z}(k+1) + \mathbf{L}_z\left[\mathbf{y}^{\alpha\beta}(k+1) - \mathbf{C}_z^{\alpha\beta}\,\overset{-\alpha\beta}{\mathbf{N}_z}(k+1)\right] \tag{45}$$

where $\mathbf{N}_z = [\mathbf{x}^{\alpha\beta T}, \mathbf{h}_1^{\alpha\beta T}, \mathbf{h}_5^{\alpha\beta T}, \mathbf{h}_7^{\alpha\beta T}, \mathbf{h}_{11}^{\alpha\beta T}, \mathbf{h}_{13}^{\alpha\beta T}]^T$

$$\mathbf{A}_{zi}^{\alpha\beta} = \begin{bmatrix} \mathbf{A}_{di}^{\alpha\beta} & \mathbf{D}_{di}^{\alpha\beta} & \mathbf{D}_{di}^{\alpha\beta} & \mathbf{D}_{di}^{\alpha\beta} & \mathbf{D}_{di}^{\alpha\beta} & \mathbf{D}_{di}^{\alpha\beta} \\ 0 & \mathbf{e}_{h1} & \mathbf{0} & \mathbf{0} & \mathbf{0} & \mathbf{0} \\ \mathbf{0} & \mathbf{0} & \mathbf{e}_{h5} & \mathbf{0} & \mathbf{0} & \mathbf{0} \\ \mathbf{0} & \mathbf{0} & \mathbf{0} & \mathbf{e}_{h7} & \mathbf{0} & \mathbf{0} \\ \mathbf{0} & \mathbf{0} & \mathbf{0} & \mathbf{0} & \mathbf{e}_{h11} & \mathbf{0} \\ \mathbf{0} & \mathbf{0} & \mathbf{0} & \mathbf{0} & \mathbf{0} & \mathbf{e}_{h13} \end{bmatrix}, \mathbf{L}_z = \begin{bmatrix} \mathbf{L}_e \\ \mathbf{L}_1 \\ \mathbf{L}_h \end{bmatrix}, \mathbf{B}_{zi}^{\alpha\beta} = \begin{bmatrix} \mathbf{B}_{di}^{\alpha\beta} \\ \mathbf{0} \end{bmatrix}, \mathbf{D}_{zi}^{\alpha\beta} = \begin{bmatrix} \mathbf{D}_{di}^{\alpha\beta} \\ \mathbf{0} \end{bmatrix}, \mathbf{d}_z^{\alpha\beta} = \begin{bmatrix} \mathbf{d}^{\alpha\beta} \\ \mathbf{0} \end{bmatrix}, \mathbf{C}_z^{\alpha\beta} = \left[\mathbf{C}_d^{\alpha\beta}\mathbf{0}\right]$$

for $i = 1, 2, \cdots, 8$, $\mathbf{e}_{hm} = \begin{bmatrix} 2\cos(m\tilde{\omega}T_s) & 1 \\ -1 & 0 \end{bmatrix}$, $\mathbf{L}_z$ denotes the LMI-based observer gain and $\mathbf{L}_e$ denotes state observer gain. The estimation state $\hat{\mathbf{N}}_{zi}^{\alpha\beta}$ is obtained by $\mathbf{y}^{\alpha\beta}$ and first estimated state $\bar{\mathbf{N}}_{zi}^{\alpha\beta}$ at the step $(k+1)T_s$.

The disturbance observer is also designed for the purpose of improving the estimation performance of LMI-based observers as follows:

$$\hat{\mathbf{d}}_z^{\alpha\beta}(k+1) = \hat{\mathbf{d}}_z^{\alpha\beta}(k) + \mathbf{L}_d\left[\mathbf{d}_z^{*\alpha\beta}(k) - \hat{\mathbf{d}}_z^{\alpha\beta}(k)\right] \tag{46}$$

$$\mathbf{d}_z^{*\alpha\beta}(k) = \mathbf{N}_z^{*\alpha\beta}(k) - \hat{\mathbf{N}}_z^{\alpha\beta}(k) \tag{47}$$

where $\mathbf{N}_z^{*\alpha\beta} = \left[\mathbf{x}_d^{*\alpha\beta T}, \hat{\mathbf{h}}_1^{\alpha\beta T}, \hat{\mathbf{h}}_5^{\alpha\beta T}, \hat{\mathbf{h}}_7^{\alpha\beta T}, \hat{\mathbf{h}}_{11}^{\alpha\beta T}, \hat{\mathbf{h}}_{13}^{\alpha\beta T}\right]^T$ and $\mathbf{L}_d$ denotes a gain of the disturbance observer. An error is derived by subtracting the LMI-based observer in (44) and (45) and a disturbance observer in (46) and (47) from the system model in (9) to yield

$$\begin{bmatrix} \mathbf{N}_z^{\alpha\beta}(k+1) - \hat{\mathbf{N}}_z^{\alpha\beta}(k+1) \\ \mathbf{d}_z^{\alpha\beta}(k+1) - \hat{\mathbf{d}}_z^{\alpha\beta}(k+1) \end{bmatrix} = \begin{bmatrix} \mathbf{A}_{zi}^{\alpha\beta} - \mathbf{L}_z\mathbf{C}_z^{\alpha\beta}\mathbf{A}_{zi}^{\alpha\beta} & \mathbf{I} - \mathbf{L}_z\mathbf{C}_z^{\alpha\beta} \\ -\mathbf{L}_d & \mathbf{I} - \mathbf{L}_d \end{bmatrix} \begin{bmatrix} \mathbf{N}_z^{\alpha\beta}(k) - \hat{\mathbf{N}}_z^{\alpha\beta}(k) \\ \mathbf{d}_z^{\alpha\beta}(k) - \hat{\mathbf{d}}_z^{\alpha\beta}(k) \end{bmatrix} \tag{48}$$

or

$$\mathbf{z}_e(k+1) = \boldsymbol{\eta}\,\mathbf{z}_e(k). \tag{49}$$

The Lyapunov function $\boldsymbol{\nu}(k)$ is defined to obtain the observer gain set as

$$\boldsymbol{\upsilon}(k) = \mathbf{z}_e^T(k)\mathbf{W}\,\mathbf{z}_e(k) \tag{50}$$

where $\mathbf{W} = \begin{bmatrix} \mathbf{W}_1 & \mathbf{0} \\ \mathbf{0} & \mathbf{W}_2 \end{bmatrix}$ is the weighting matrix. To ensure the stable observer, (50) should monotonically decrease, i.e., $\boldsymbol{\upsilon}(k+1) < \boldsymbol{\upsilon}(k)$. It leads the LMI as below [16]

$$\boldsymbol{\eta}^T\mathbf{W}\,\boldsymbol{\eta} < \mathbf{W} < \zeta^2\mathbf{W} = \mathbf{W}_0 \tag{51}$$

or

$$\mathbf{W}_0 - \boldsymbol{\eta}^T(\mathbf{W}\mathbf{W}^{-1})\mathbf{W}\,\boldsymbol{\eta} > 0 \tag{52}$$

where the convergence rate $\zeta$ $(0 < \zeta < 1)$ minimizes the Lyapunov function to determine the optimal observer gains. Applying the Schur complement yields

$$\underset{\mathbf{W}_0,\ \mathbf{W}}{\mathbf{MIN}}\ \zeta \quad \text{subject to} \begin{bmatrix} \mathbf{W}_0 & \gamma^{-1} \\ \gamma & \mathbf{W} \end{bmatrix} \geq 0 \tag{53}$$

where $\gamma = \begin{bmatrix} \mathbf{W}_1\mathbf{A}_{zi}^{\alpha\beta} - \mathbf{Y}_z\mathbf{C}_z^{\alpha\beta}\mathbf{A}_{zi}^{\alpha\beta} & \mathbf{W}_1 - \mathbf{Y}_z\mathbf{C}_z^{\alpha\beta} \\ -\mathbf{Y}_d & \mathbf{W}_2 - \mathbf{Y}_d \end{bmatrix}$.

Then, the LMI-based observer gains are obtained as $\mathbf{L}_z = \mathbf{W}_1^{-1}\mathbf{Y}_z$ and the disturbance observer gains are as $\mathbf{L}_d = \mathbf{W}_2^{-1}\mathbf{Y}_d$. In this paper, the LMI method is solved by using MATLAB toolbox SeDuMi version 1.1 [22] and YALMIP version R20180413 [23]. The proposed LMI-based observer ensures zero estimation error at the steady state even under frequency fluctuation and grid distortion.

*4.2. Frequency Estimation*

From the estimates of the utility grid voltage, the grid frequency and phase angle are directly extracted by using a MAF-PLL [20] to realize the synchronization process without the use of grid voltage sensors. In general, the controller and observer performances are severely influenced by the accuracy of the estimated frequency of the utility grid. To prevent the performance degradation caused by the grid frequency fluctuation, the estimated grid frequency is adaptively updated.

By using the MAF, the filtered grid frequency is represented as follows:

$$\widetilde{\omega}\ (k) = \frac{1}{M}\sum_{i=0}^{M-1}\hat{\omega}\ (k-i) \tag{54}$$

where $\hat{\omega}$ is the grid angular frequency estimate by the estimated grid voltages, $\widetilde{\omega}$ is the filtered frequency, and $M$ is the number of samples in window. Also, the phase delay is compensated by an adaptive delay compensator.

## 5. Stability Analysis

The stability of the proposed control scheme is investigated under the variation of the grid impedance and parametric uncertainties. The proposed control achieves excellent tracking performance as well as strong robustness under weak grid. The eigenvalue locations and frequency responses are presented in the $z$-domain. Since the proposed current controller is designed in the '$dq$' frame while the LMI-based observer is designed in the '$\alpha\beta$' frame in the proposed scheme, the eigenvalues are investigated separately.

*5.1. Eigenvalue Map*

Figure 3a,b show the eigenvalue plots for the proposed EMPC scheme and the proposed LMI-based observer under the filter parametric uncertainties. It is noted that the grid impedance variation due to weak grid is included in $L_2$ variation. It is confirmed from these figures that all the eigenvalues maintain inside the stable region despite the changes in filter parameters. This effectively proves the robustness of the proposed control method.

*5.2. Frequency Responses*

Figure 4 shows the frequency responses of the proposed EMPC scheme for the reference tracking performance and disturbance rejection under parametric uncertainties. Frequency responses are obtained for all vertices of the polytopic system model. Similar to Figure 3, the effect of grid impedance is considered by the variation of $L_2$. In other words, $L_2$ is represented as sum of the nominal $L_2$ and $L_g$ under grid impedance. However, the impact of the proposed LMI-based adaptive observer and PR controller are not taken into account. It is clearly confirmed by Figure 4 that the proposed EMPC method provides a superior reference tracking as well as complete disturbance rejection capability.

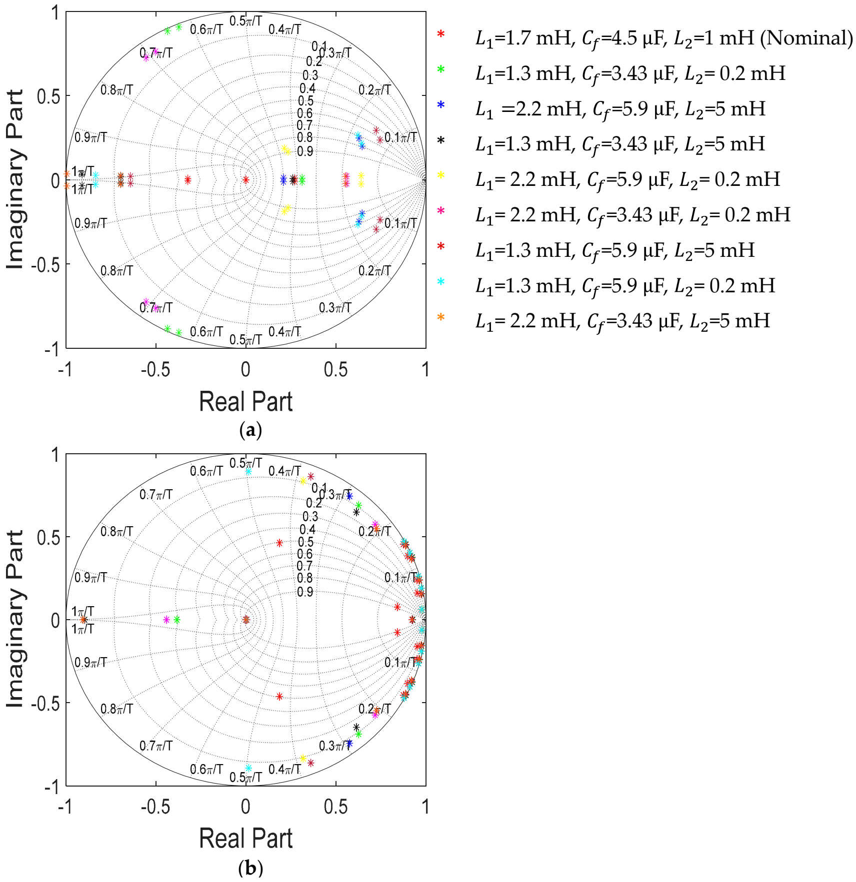


**Figure 3.** Eigenvalues with LCL parametric uncertainties. (**a**) The proposed EMPC. (**b**) The proposed LMI-based observer.

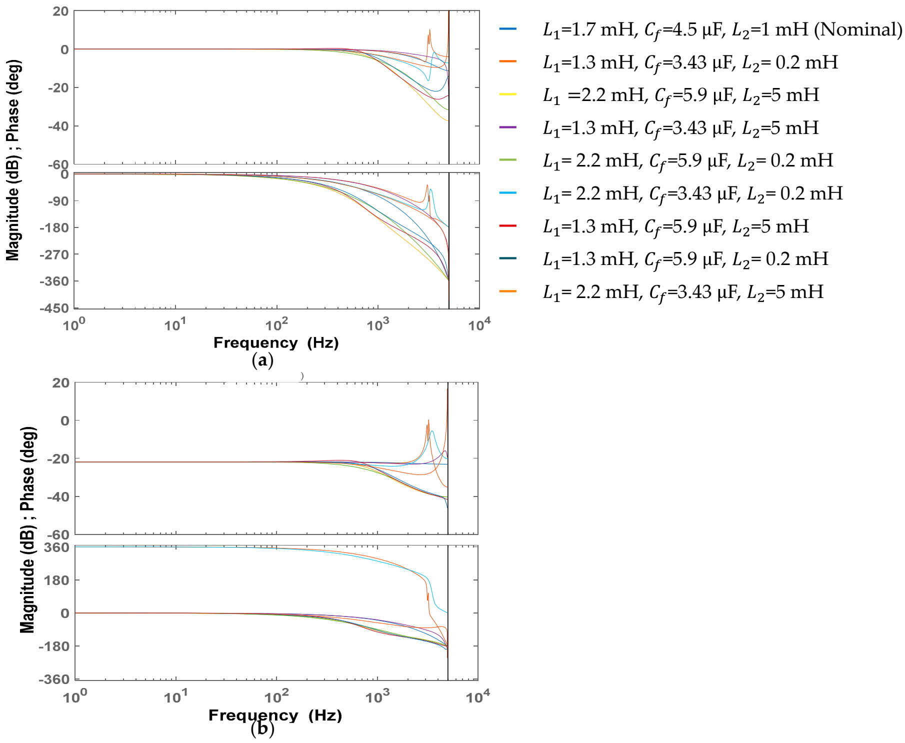


**Figure 4.** Frequency responses of the proposed EMPC scheme under LCL parametric uncertainties. (**a**) Reference tracking response. (**b**) Disturbance rejection response.

## 6. Simulation Validation

To validate the effectiveness of the proposed scheme, simulations are conducted for a three-phase GCI prototype. The parameters of the GCI and utility grid are represented in Table 1. The proposed control method is evaluated under the 5th, 7th, 11th, and 13th grid voltage harmonic components with 5% of the fundamental grid voltage magnitude.

**Table 1.** Parameters of the GCI and utility grid.

| Parameters | Value | Units |
|---|---|---|
| Filter resistance | 0.5 | Ω |
| Filter capacitance | 1/4.5/6 | μF |
| Inverter-side inductance | 1.7 | mH |
| Grid-side inductance | 1.0 | mH |
| Grid voltage | 220 | V |
| Grid frequency | 50/60 | Hz |
| Grid inductance | 4.0 | mH |
| Switching frequency | 10 | kHz |
| DC-link voltage | 420 | V |

Figure 5 represents the grid current responses produced by the proposed control method by the simulation when the utility grid voltages include distortion and frequency change. The waveform in Figure 5a shows the high-quality grid currents even under harsh disturbance from the grid. Figure 5b shows the current responses when additional grid impedance ($L_g$ = 4 mH) is applied in addition to distorted grid voltages and frequency change from 60 Hz to 50 Hz at 0.6 s. The results of Figure 5 demonstrate that the proposed current controller ensures strong robustness and good control response under voltage distortion of the utility grid, grid frequency change, and grid impedance uncertainty.

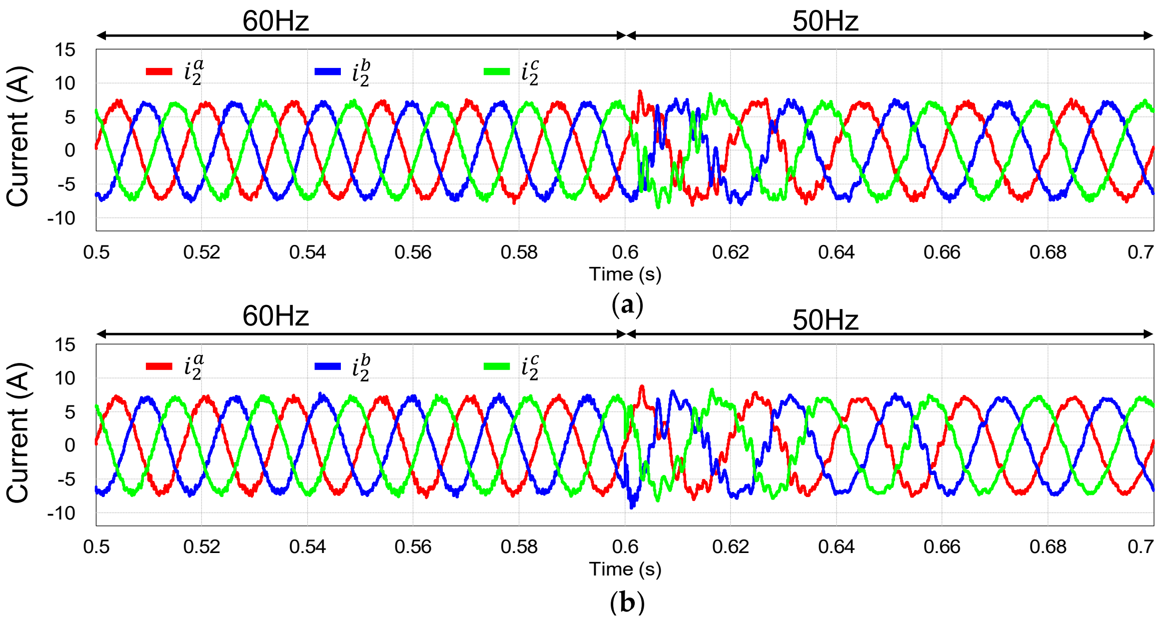


**Figure 5.** Simulation for the proposed method. (**a**) Grid currents under grid voltage distortion and frequency change. (**b**) Grid currents under grid voltage distortion and frequency change with the grid impedance of $L_g$ = 4 mH.

Reliable inverter operation without using the grid voltage sensors is mainly dependent on the estimating performance of the utility grid voltages. Figure 6 evaluates the estimating performance of the proposed LMI-based observer designed in αβ frame by simulation results by comparing the estimated states with measured states or references. The estimated and measured states for the grid currents are presented in Figure 6a, the estimated and reference inverter currents in Figure 6b, the estimated and reference capacitor voltages in Figure 6c, and the estimated and measured gird voltages in Figure 6d. It is confirmed that the proposed LMI-based observer ensures stability and estimating capability.

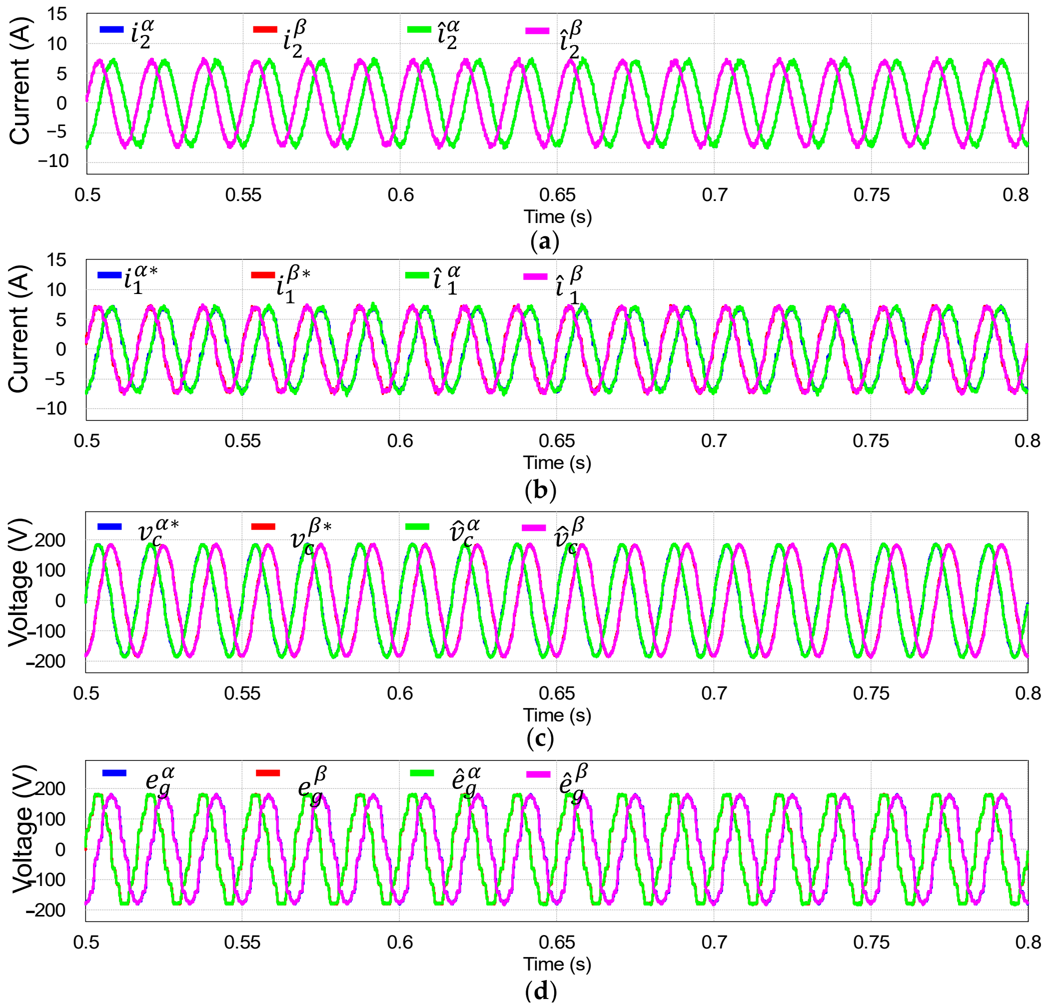


**Figure 6.** Simulation for LMI-based observer under grid voltage distortion in αβ frame. (**a**) Estimated and measured grid currents. (**b**) Estimated and reference inverter currents. (**c**) Estimated and reference capacitor voltages. (**d**) Estimated and measured gird voltages.

One of common challenges of a grid voltage sensorless current control scheme is the smooth start-up performance even under grid voltage distortion and imbalance. To verify the performance of the proposed scheme from the start-up instant to the steady state, the simulations are conducted under system uncertainties and grid voltage imbalance/distortion in Figure 7. Figure 7a represents the grid voltages, in which the magnitude of phase-$a$ voltage drops to 50% of the nominal voltage. Figure 7b shows the current responses of the proposed grid voltage sensorless current controller at the start-up instant at 0.05 s, in which the grid impedance with $L_g$ of 4 mH is connected between the GCI output and the main grid as shown in Figure 1. Evidently, the proposed scheme takes 60 ms to reach the steady state with low overshoot in the grid-injected currents. It is worth noting that the proposed scheme successfully removes the grid voltage sensors; thus, the dynamic of the proposed observer to estimate the grid phase angle, and unavoidable PLL delay also affect the transient performance. However, even when large power is injected from inverter to the weak grid, the inverter system still maintains stability and the proposed scheme produces the high-quality injected currents. Figure 7c shows the current responses of the proposed control scheme at the start-up instant at 0.05 s with the filter capacitance variation from 4.5 μF to 6 μF. Without severe influence from the negative effect of weak grid condition, the grid-injected currents stably reach the steady state after only 40 ms and the high-quality current is maintained even under abnormal grid conditions and internal uncertainty.

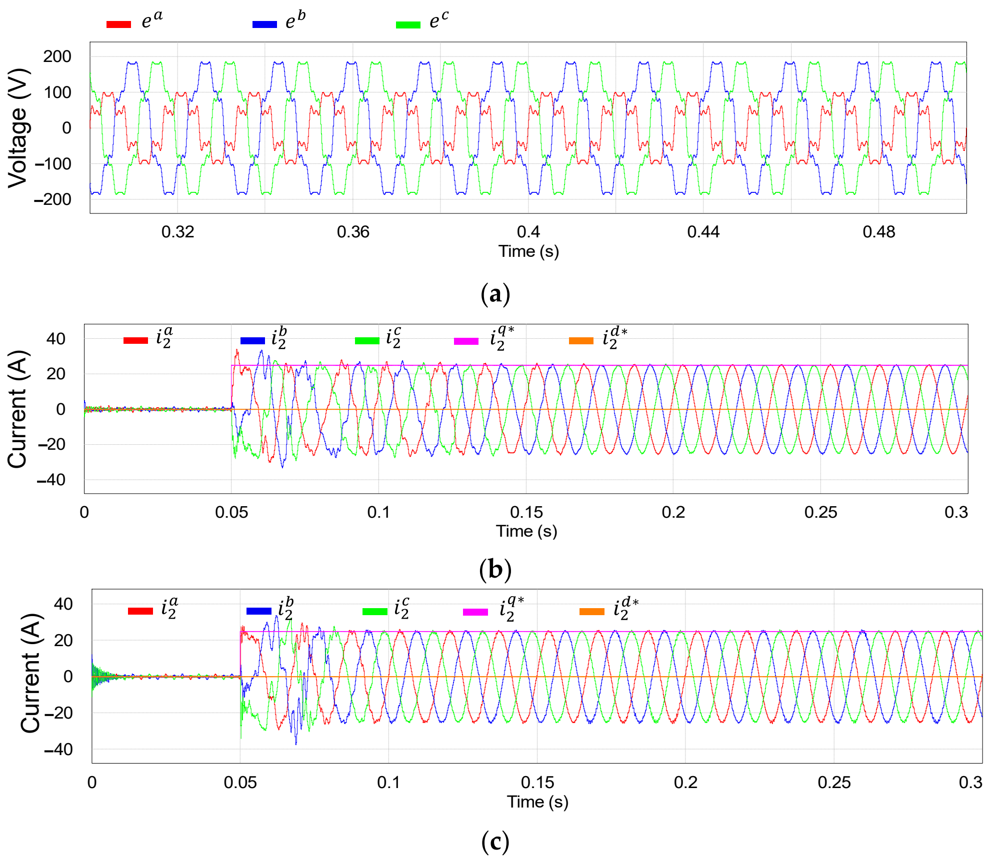


**Figure 7.** Current responses of the proposed current controller under grid voltage distortion/imbalance and the current reference of 25 A. (**a**) Grid voltages. (**b**) Current response at the start-up instant with grid inductance $L_g$ = 4 mH. (**c**) Current response at the start-up instant with filter capacitance $C_f$ = 6 μF.

Figures 8 and 9 show the comparative results between the MPC presented in [6] and the proposed controller when the grid condition and system parameters are suddenly changed. For a fair comparison of only the controller with the proposed EMPC method, the conventional MPC scheme in [6] is constructed with the same proposed LMI-based observer. Figure 8 shows the grid current responses produced by two control schemes under the grid voltage distortion and imbalance with uncertain grid impedance. Figure 9 shows the grid current responses controlled by two control schemes under the grid voltage distortion and imbalance as well as the filter parametric uncertainty. Accordingly, Figures 8a and 9a show the PCC voltages and grid voltages used in those test conditions, in which at 0.6 s, phase-*a* of grid voltage drops to 50% (drops from 180 V to 90 V). Two control methods exhibit distinct control performance. As soon as the parametric uncertainty is added to the conventional MPC, the grid-injected current quality is degraded significantly with high oscillation in phase currents as shown in Figures 8b and 9b. On the contrary, the proposed scheme effectively stabilizes the system, yielding sinusoidal currents as in Figures 8c and 9c. The comparison results clearly demonstrate that the proposed scheme ensures strong robustness against unexpected grid conditions and system uncertainty.

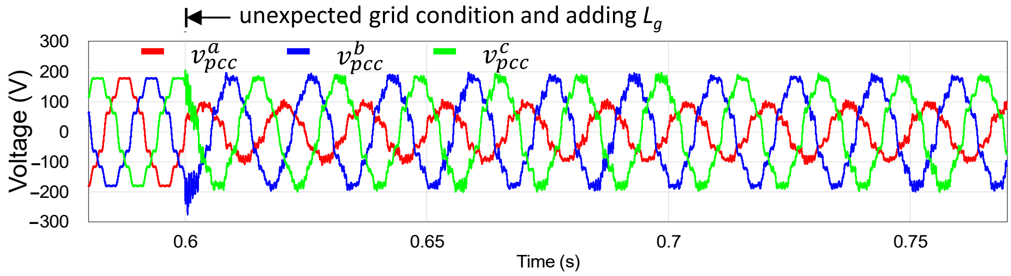


(**a**)

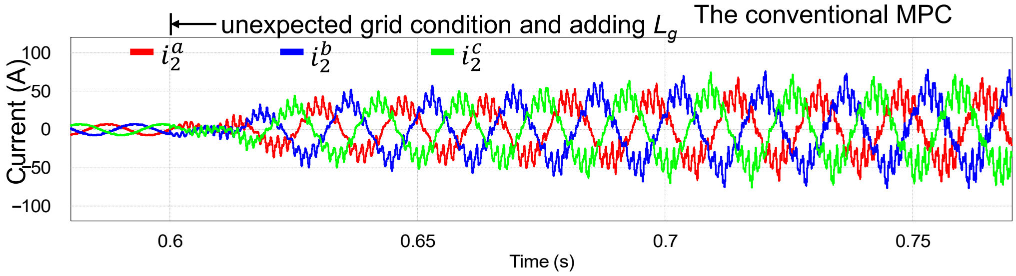


(**b**)

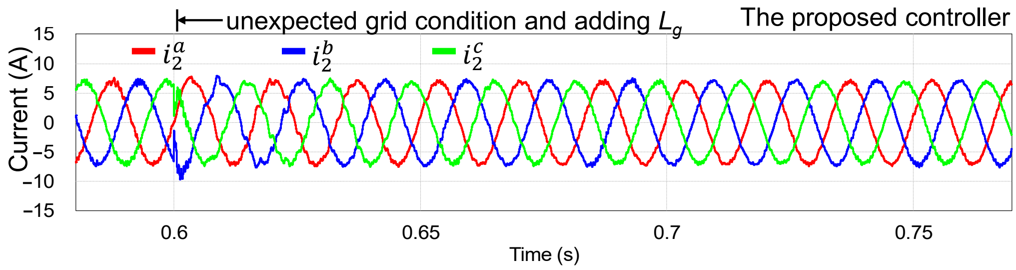


(**c**)

**Figure 8.** Comparison results between the conventional MPC in [6] and the proposed controller under unexpected grid conditions such as grid impedance ($L_g$ = 4 mH) and grid voltage distortion/imbalance ($e_a$ drops to 50% of the nominal value at 0.6 s). (**a**) PCC voltages. (**b**) Grid currents of the conventional MPC. (**c**) Grid currents of the proposed controller.

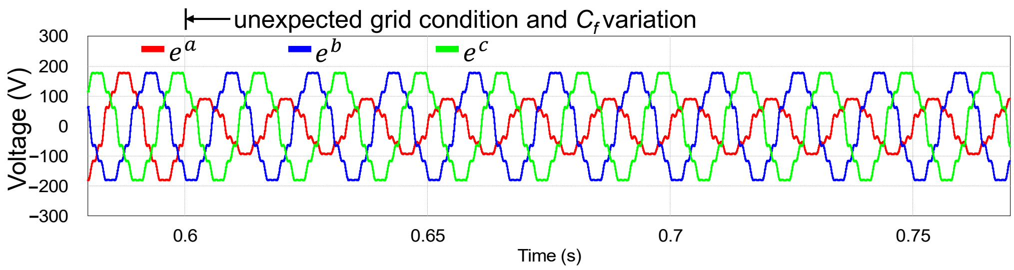


(**a**)

**Figure 9.** *Cont.*

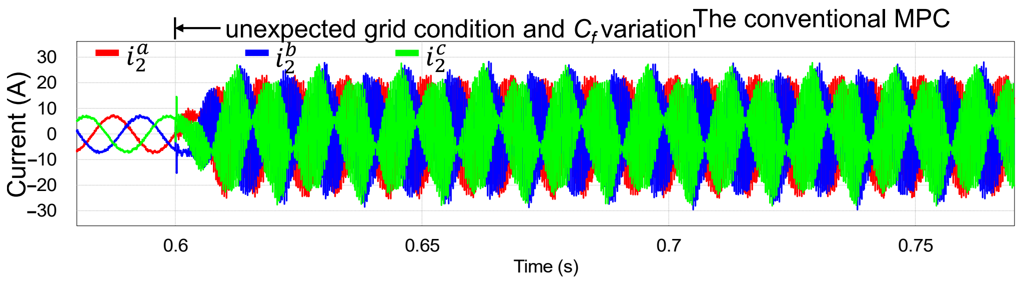


(**b**)

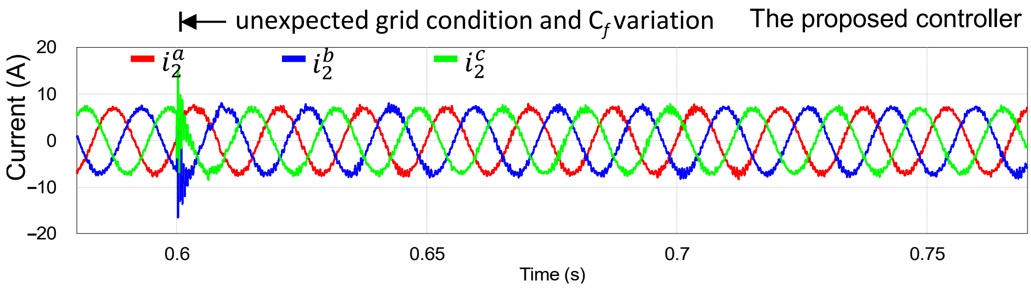


(**c**)

**Figure 9.** Comparison results between the conventional MPC in [6] and the proposed controller under system uncertainties ($C_f$ varies from 4.5 µF to 6 µF) and grid voltage distortion/imbalance ($e_a$ drops to 50% of the nominal value at 0.6 s). (**a**) Grid voltages. (**b**) Grid currents of the conventional MPC. (**c**) Grid currents of the proposed controller.

## 7. Experimental Validation

The proposed control method is executed in the lab-based experimental system to prove the performance and robustness by experiments. Figure 10 depicts the experimental test setup, in which the AC programmable power source is employed to realize the distorted and imbalanced utility grid environment. To implement the proposed EMPC-based grid voltage sensorless control, the DSP TMS320F28335 (Texas Instruments, Dallas, TX, USA) is used. To construct the system with the proposed method, DC-link voltage and grid currents in phase-$a$ and -$b$ are measured. The grid voltages are not only contaminated by harmonic distortion, but also imbalanced with $e_a$ drop to 70.56% from the nominal voltage.

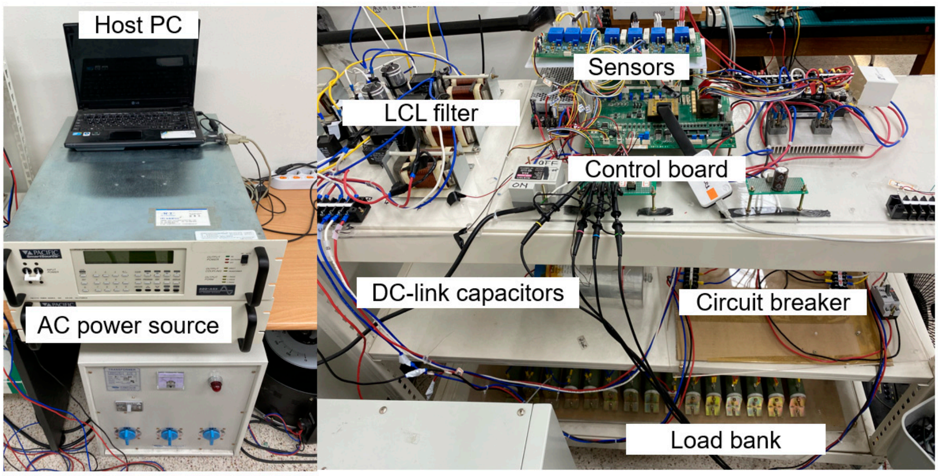


**Figure 10.** Photo of the lab-based experimental system.

Figure 11 presents the experimental comparison results for steady-state tracking performance between the conventional MPC in [6] and the proposed controller under $C_f$ uncertainty. In these figures, the grid phase angle estimates are also shown to verify the synchronization performance without grid voltage sensors. The conventional MPC in [6] and the proposed control show similar results with $C_f$ =1 µF as shown in Figure 11a,b. In contrast, the proposed control exhibits better current quality and less oscillation than the conventional one with $C_f$ = 6 µF as in Figure 11c,d.

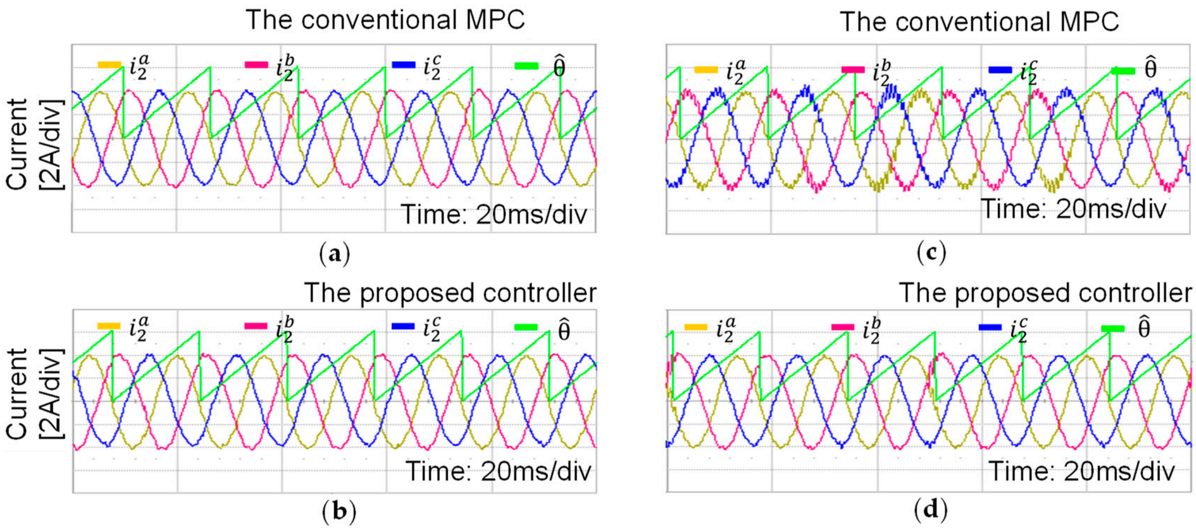


**Figure 11.** Comparative experimental results between the conventional MPC in [6] and the proposed method under system parametric uncertainties and grid voltage distortion/imbalance. (**a**) Conventional MPC with $C_f$ decrease to 1 µF. (**b**) Proposed controller with $C_f$ decrease to 1 µF. (**c**) Conventional MPC with $C_f$ increase to 6 µF. (**d**) Proposed controller with $C_f$ increase to 6 µF.

To validate the proposed control robustness under the grid impedance variation caused by a weak grid, Figure 12 represents comparative experimental results when the grid impedance with $L_g$ of 4 mH exists under imbalanced and distorted grid voltages. The phase-*a* current FFT spectrums for the proposed method are also presented in Figure 12c to assess the grid current quality. While the proposed method is stable in the presence of such severe grid disturbances, the conventional scheme becomes rapidly unstable with the same conditions before the protection algorithm is finally activated. The experimental results of Figures 11 and 12 match well with the simulation in Figures 8 and 9 in views of the system stability and the quality of grid currents.

The experimental responses in Figure 13 present the transient performance of the proposed method when the utility grid frequency rapidly changes from 60 Hz to 50 Hz. As test conditions, while the grid voltage is distorted in Figure 13a, it is distorted as well as imbalanced in Figure 13b. These results demonstrate that the grid currents are quickly restored to the sinusoidal form even under both grid frequency change and harsh grid disturbance such as imbalance and distortion, which well matches the simulation results in Figure 5. Additionally, the grid frequency estimated by using the MAF-PLL from the estimated grid voltages rapidly tracks new frequency value without a noticeable overshoot. All experimental tests clearly verify the robustness and performance of the proposed method which produces stable and pure sinusoidal grid current even under weak grid and parametric uncertainty without using the measurement of the grid voltages.

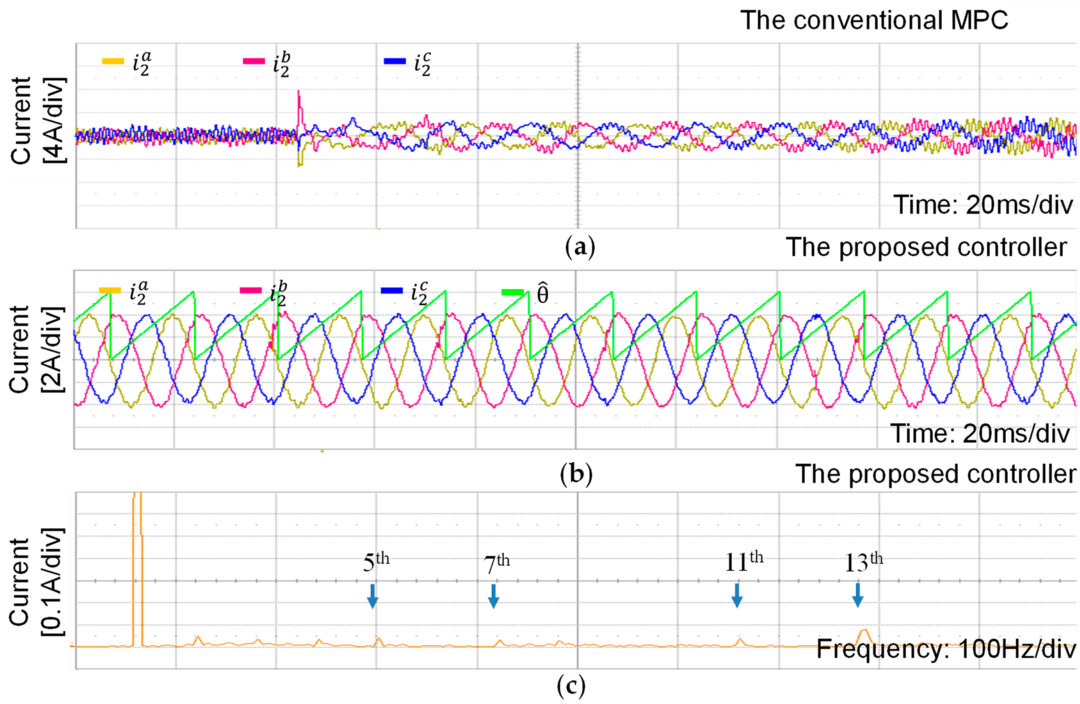


**Figure 12.** Comparative experimental results between the conventional MPC in [6] and the proposed method under grid voltage distortion/imbalance with grid impedance ($L_g$ = 4 mH). (**a**) Conventional MPC. (**b**) Proposed controller. (**c**) FFT of phase-*a* current with the proposed controller.

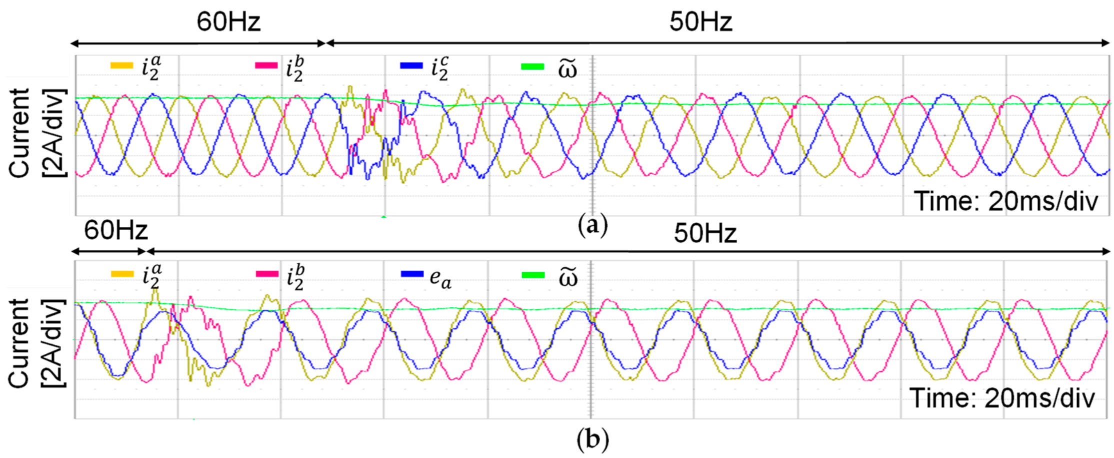


**Figure 13.** Experimental results of the proposed method. (**a**) Estimated frequency and grid currents under grid voltage distortion and frequency change. (**b**) Estimated frequency, measured phase-*a* grid voltage, and grid currents under voltage distortion/imbalance and frequency change of the utility grid.

## 8. Conclusions

This paper presents a robust EMPC-based frequency-adaptive current control combined with the LMI approach without using grid voltage sensors for the GCI with an LCL filter in the presence of parametric uncertainties and abnormal utility grid. The main contributions of this paper can be summarized as follows:

(i) The LMI-based MPC algorithm has been employed by an LQR-based prediction model in order to achieve zero-reference tracking error even under grid voltage imbalance and negative effects from parametric uncertainties. The resonant controllers with the grid frequency-adaptive capability have been adopted to effectively compensate the distorted grid harmonics under grid frequency fluctuations.

(ii) In order to realize a current controller without the grid voltage sensors, the proposed controller employs a frequency-adaptive LMI-based resonant extended state observer to guarantee high estimation accuracy for grid voltages and system state variables under abnormal and unexpected grid conditions. Also, the proposed LMI-based observer also integrates a disturbance observer to ensure a good performance of the resonant extended state observer by rejecting the influence of disturbances.

(iii) The eigenvalue maps and frequency responses of the nominal system and parametric uncertain systems have been evaluated to validate the stability and robustness of the proposed current control scheme.

The proposed control scheme for GCI without using the grid voltage sensor has been validated by conducting both simulations based on PSIM software (9.1, Powersim, Rockville, MD, USA) and experiments based on a lab-based testbed. Comprehensive simulation and experimental results have effectively validated the control robustness of the proposed scheme under several adverse conditions such as internal parametric uncertainties as well as unexpected distorted and imbalanced grid.

**Author Contributions:** Y.K., T.V.T. and K.-H.K. developed the basic idea for the system and controller design and synthesis, and investigated the total system structure. Y.K. analyzed the system based on the numeric simulation data with the supervision from K.-H.K. T.V.T. conducted the literature survey and simulations. Y.K., T.V.T. and K.-H.K. worked together to prepare the manuscript. All authors have read and agreed to the published version of the manuscript.

**Funding:** This research was supported by Basic Science Research Program through the National Research Foundation of Korea (NRF) funded by the Ministry of Education (NRF-2019R1A6A1A03032119). This work was supported by the National Research Foundation of Korea (NRF) grant funded by the Korea government (MSIT) (NRF-2022R1F1A1064350).

**Data Availability Statement:** Data are contained within the article.

**Conflicts of Interest:** The authors declare no conflicts of interest.

## References

1. Yang, H.; Zhang, Y.; Liang, J.; Gao, J.; Walker, P.D.; Zhang, N. Sliding-mode observer based voltage-sensorless model predictive power control of PWM rectifier under unbalanced grid conditions. *IEEE Trans. Ind. Electron.* **2018**, *65*, 5550–5560. [CrossRef]
2. Carrasco, J.; Franquelo, L.; Bialasiewicz, J.; Galvan, E.; Guisado, R.; Prats, M.; Leon, J.; Moreno-Alfonso, N. Power-electronic systems for the grid integration of renewable energy sources: A survey. *IEEE Trans. Ind. Electron.* **2006**, *53*, 1002–1016. [CrossRef]
3. Trinh, Q.N.; Lee, H.H. An advanced current control strategy for three-phase shunt active power filters. *IEEE Trans. Indus. Electr.* **2013**, *60*, 5400–5410. [CrossRef]
4. Abu-Rub, H.; Malinowski, M.; Al-Haddad, K. *Power Electronics for Renewable Energy Systems, Transportation and Industrial Applications*; John Wiley & Sons: Hoboken, NJ, USA, 2014.
5. *IEEE Std. 1547.2-2008*; IEEE Application Guide for IEEE Std. 1547, IEEE Standard for Interconnecting Distributed Resources with Electric Power Systems. IEEE: New York, NY, USA, 2008.
6. Kim, Y.; Tran, T.V.; Kim, K.-H. LMI-based model predictive current control for an LCL-filtered grid-connected inverter under unexpected grid and system uncertainties. *Electronics* **2022**, *11*, 731. [CrossRef]
7. Jalili, K.; Bernet, S. Design of LCL filters of active-front-end two-level voltage-source converters. *IEEE Trans. Ind. Electron.* **2009**, *56*, 1674–1689. [CrossRef]
8. Rodriguez-Diaz, E.; Freijedo, F.D.; Vasquez, J.C.; Guerrero, J.M. Analysis and comparison of notch filter and capacitor voltage feedforward active damping techniques for LCL grid-connected converters. *IEEE Trans. Power Electron.* **2018**, *34*, 3958–3972. [CrossRef]
9. Yoon, S.J.; Lai, N.B.; Kim, K.-H. A systematic controller design for a grid-connected inverter with LCL filter using a discrete-time integral state feedback control and state observer. *Energies* **2018**, *11*, 437. [CrossRef]
10. Jia, Y.; Zhao, J.; Fu, X. Direct grid current control of LCL-filtered grid-connected inverter mitigating grid voltage disturbance. *IEEE Trans. Power Electron.* **2014**, *29*, 1532–1541.
11. Bimarta, R.; Kim, K.-H. A robust frequency-adaptive current control of a grid-connected inverter based on LMI-LQR under polytopic uncertainties. *IEEE Access* **2020**, *8*, 28756–28773. [CrossRef]
12. Da Ponte Caun, R.; Assuncao, E.; Teixeira, M.C.M. H2/H∞ formulation of LQR controls based on LMI for continuous-time uncertain systems. *Int. J. Sys. Sci.* **2020**, *52*, 612–634. [CrossRef]
13. De Matos, J.G.; E Silva, F.S.F.; Ribeiro, L.A.D.S. Power control in AC isolated microgrids with renewable energy sources and energy storage systems. *IEEE Trans. Ind. Electron.* **2015**, *62*, 3490–3498.

14. Han, H.; Hou, X.; Yang, J.; Wu, J.; Su, M.; Guerrero, J.M. Review of power sharing control strategies for islanding operation of AC microgrids. *IEEE Trans. Smart Grid.* **2016**, *7*, 200–215. [CrossRef]
15. Gao, J.; Gong, C.; Li, W.; Liu, J. Novel compensation strategy for calculation delay of finite control set model predictive current control in PMSM. *IEEE Trans. Ind. Electron.* **2020**, *67*, 5816–5819. [CrossRef]
16. Nam, N.N.; Nguyen, N.-D.; Yoon, C.; Lee, Y.I. Disturbance observer-based robust model predictive control for a voltage sensorless grid-connected inverter with an LCL filter. *IEEE Access* **2021**, *9*, 109793–109805. [CrossRef]
17. Tran, T.V.; Yoon, S.J.; Kim, K.-H. An LQR-based controller design for an LCL-filtered grid-connected inverter in discrete-time state-space under distorted grid environment. *Energies* **2018**, *11*, 2062. [CrossRef]
18. Bimarta, R.; Tran, T.V.; Kim, K.-H. Frequency-adaptive current controller design based on LQR state feedback control for a grid-connected inverter under distorted grid. *Energies* **2018**, *11*, 2674. [CrossRef]
19. Lai, N.B.; Kim, K.-H. Robust control scheme for three-phase grid-connected inverters with LCL-filter under unbalanced and distorted grid conditions. *IEEE Trans. Energy Conver.* **2017**, *33*, 506–515. [CrossRef]
20. Golestan, S.; Ramezani, M.; Guerrero, J.M.; Freijedo, F.D.; Monfared, M. Moving average filter based phase-locked loops: Performance analysis and design guidelines. *IEEE Trans. Power Electron.* **2014**, *29*, 2750–2763. [CrossRef]
21. Tran, T.V.; Kim, K.-H. Frequency adaptive grid voltage sensorless control of LCL-filtered inverter based on extended model observer. *IEEE Trans. Ind. Electron.* **2020**, *67*, 7560–7573. [CrossRef]
22. Sturm, J.F. Using SeDuMi 1.02, a MATLAB toolbox for optimization over symmetric cones. *Optim. Method Softw.* **1999**, *11*, 625–653. [CrossRef]
23. Lofberg, J. YALMIP: A toolbox for modeling and optimization in MATLAB. In Proceedings of the IEEE International Symposium on Computer-Aided Control System Design, Taipei, Taiwan, 2–4 September 2004; pp. 284–289.